INORGANIC CHEMISTRY FRONTIERS

RESEARCH ARTICLE

View Article Online
View Journal | View Issue

Cite this: *Inorg. Chem. Front.*, 2025, **12**, 4623

H/OH substitution, construction of K–O coordinated bonds and introduction of homochirality for the design of a 3D hybrid double perovskite multiferroic†

Mei-Ling Ren, Ze-Jiang Xu, Hua-Kai Li, Zi-Ao Qiu, Liang-Han Shen, Xiang Zhang, Chao Shi, Na Wang, * Heng-Yun Ye * and Le-Ping Miao *

Three-dimensional (3D) hybrid metal-halogen perovskite multiferroic materials have great advantages in the application of ferroic-photoelectric devices because of their excellent physical properties, including ferroelectricity, ferroelasticity, large piezoelectric response, and high carrier mobility. Currently, relatively few types of 3D hybrid metal-halogen perovskite multiferroic materials are known, as their construction requires their organic structure to conform to the Goldschmidt tolerance factor. Moreover, their performance potential is limited by their lower Curie temperature (T_c). Herein, we successfully designed a novel 3D hybrid double perovskite (R-3P)$_2$KBiCl$_6$ (R-3P = (R)-3-hydroxypyrrolidinium, R3PBKC) using the synthesis strategy of generating K–O coordination bonds through H/OH substitution and introducing homochirality. Notably, R3PBKC exhibited an unusually high T_c (376 K) structural phase transition of $P1$–$P1$–$P2_1$–$P6_322$, and the ferroelectric–ferroelastic multiferroicity of R3PBKC was verified using typical polarization electric field (P–E) hysteresis loops and temperature-dependent evolution of ferroelastic domains. This study presents a simple and efficient molecular strategy to realize the construction of 3D hybrid perovskite ferroelectrics, opening up a new research path for the design and development of 3D multiferroic materials.

Received 10th February 2025,
Accepted 29th March 2025

DOI: 10.1039/d5qi00399g

rsc.li/frontiers-inorganic

1. Introduction

Multiferroics are multifunctional materials exhibiting ferroelectric (FE), ferroelastic (FA), ferromagnetic (FM), and antiferromagnetic (AFM) properties.[1–8] They have broad applications in memory, actuators, energy conversion, information storage, photoelectric devices, and sensors.[9–16] Organic–inorganic hybrid perovskites (OIHPs) have many advantages for developing ferroic order materials, such as mechanical flexibility, environmental friendliness, and structural tunability.[17–24] Among them, 3D OIHPs have been widely studied for their high absorption coefficient, high defect tolerance, and superior photoelectric performance, accelerating the advancement of technologies such as solar cells, photoelectric semiconductors, and X-ray photodetectors.[25–30] For example, $[CH_3NH_3]PbI_3$ has excellent photovoltaic properties and is considered a future high-performance and low-cost light harvesting material.[31] However, the ionic radius of the organic cations in 3D perovskites must satisfy the Goldschmidt tolerance factor $\tau = (r_A + r_X)/\sqrt{2}(r_B + r_X)$ (r is the ionic radius), which poses a significant challenge in the development of 3D OIHPs.[32–35]

Practicable molecular strategies in "ferroelectrochemistry" have been proposed for the targeted design of ferroelectricity, such as homochirality introduction, H/F substitution, and the quasi-spherical strategy.[36–39] For example, introducing chirality into hybrid perovskites restricts their symmetry to chiral point groups, including C_1, C_2, D_2, C_3, D_3, C_4, D_4, C_6, D_6, T, and O, among which 5 of the 11 chiral point groups are polar point groups (C_1, C_2, C_3, C_4, C_6).[40–42] Thus, introducing homochirality is an effective strategy to achieve ferroelectricity or multiferroicity. For instance, the first reported two-dimensional (2D) ferroelectric–ferroelastic multiferroic (R/S)-N-((1-phenylethyl) ethane-1,2-diamine)PbI_4 based on the non-ferroelectric perovskite (N-benzylethane-1,2-diaminium)PbI_4 was successfully obtained by introducing homochirality.[43] In addition, H/F substitution has been recognized as an effective way to achieve ferroelectricity, such as in the case of the ferroelectric [FMeTP][Ni$(NO_2)_3$] (FMeTP = N-fluoromethyltropine), which was success-

Chaotic Matter Science Research Center, Department of Materials, Metallurgy and Chemistry, Jiangxi University of Science and Technology, Ganzhou 341000, P.R. China. E-mail: miaoleping@jxust.edu.cn

†Electronic supplementary information (ESI) available: Synthesis and measurement, including TGA, powdered XRD patterns, PFM, second harmonic generation, piezoelectric measurement. CCDC 2412865–2412871. For ESI and crystallographic data in CIF or other electronic format see DOI: https://doi.org/10.1039/d5qi00399g

fully obtained *via* an H/F substitution strategy based on non-ferroelectric $[(CH_3)_4N][Ni(NO_2)_3]$.[44] Therefore, modification of organic components is an effective approach to realize ferroelectricity. However, the regulation of ferroelectricity *via* H/OH substitution on organic cations is still poorly understood.

In fact, H/OH substitution shows the advantages of introducing chirality and enhancing internal molecular interactions. The molecular ferroelectric [quinuclidine]$GaCl_4$ was transformed into the molecular multiferroic (R3HQ)$GaCl_4$ (R3HQ = (*R*)-3-hydroxylquinuclidinium) through the H/OH substitution strategy.[45] Moreover, it can form coordinated bonds like K–O, and Rb–O to control the molecular structure/symmetry. For example, 3D double-metal perovskite $(MEPRD)_2MBiX_6$(MEPRD = 1-methylpyrrolidin-1-ium-3-ol, M = K and Rb, X = Cl and Br) with characteristics of semiconductor.[46] Considering the above advantages, we designed a 3D multiferroic $(R\text{-3P})_2KBiCl_6$ (*R*-3P = (*R*)-3-hydroxypyrrolidinium, R3PBKC) and ferroelastic $(3P)_2KBiCl_6$ (3PBKC, 3P = 3-hydroxypyrrolidinium) through H/OH substitution from the non-ferroic one-dimensional (1D) hybrid perovskite $(pyrrolidinium)_2BiCl_3$ (PBC) and $(3\text{-methylpyrrolidine})_2KBiCl_6$ (3MPBKC). Interestingly, H/OH substitution generates K–O coordinated bonds forming a novel 3D structure. At the same time, it introduces homochirality reducing the structural symmetry (Scheme 1). As expected, R3PBKC crystallizes in space group *P*1 with a T_c of 392 K. In addition, R3PBKC has an abnormal *P*1–*P*1–$P2_1$–$P6_322$ phase transition showing ferroelectric–ferroelastic multiferroicity, with a spontaneous polarization P_s of 3.75 μC cm^{-2}, along with semiconducting properties. This work not only enriches the 3D hybrid double-metal perovskite multiferroics compound family but also provides a promising design strategy for hybrid perovskite ferroelectrics.

2. Results and discussion

2.1. Crystal structure analysis

The colorless single crystals of PBC, 3MPBKC, 3PBKC, and R3PBKC were obtained by slow solution evaporation, and the phase purity of the four compounds was verified by powder X-ray diffraction (PXRD) (Fig. S1†). Thermogravimetry analysis (TGA) shows that R3PBKC remains stable below 507 K (Fig. S2†). All the single-crystal structures were characterized by X-ray single-crystal diffractions, where PBC was collected at 300 K, 3MPBKC (268 K), 3PBKC (300 K), and R3PBKC at 302, 353, 386 and 413 K, respectively. The compounds PBC and 3MPBKC crystallize in the non-polar space groups *Pnma* and *C*2/*m*, respectively, exhibiting 1D hybrid perovskite structures (Table S1†). Both PBC and 3MPBKC exhibit a sandwich-like structure, in which a one-dimensional inorganic skeleton is intermingled with a layer of organic cations (Fig. S3†). After H/OH substitution, the 3D perovskite structure was formed by K–O coordinated bonds. As a result, 3PBKC crystallizes in the monoclinic polar space group *Cc* with the point group *m* (C_{1h}). The cell parameters are a = 8.4070(4) Å, b = 17.4670(9) Å, c = 13.4096(6) Å, $\alpha = \gamma = 90°$, β = 93.585(5)°, and V = 1965.28(17) $Å^3$ (Table S1†). Its minimum asymmetric unit consists of two 3P organic cations and one $[KBiCl_6]^{2-}$ ion. The complex connections form a 3D caged framework, with the organic cation 3P filling its cavity. When the homochirality was introduced, a similar 3D structural R3PBKC was obtained. Significantly, R3PBKC adopts the lowest-symmetric crystal system, with space group *P*1.

To clarify the mechanism of the structural phase transition (SPT), and the origin of spontaneous polarization at the molecular level, the crystal structures of all phases of R3PBKC were analyzed. In the low-temperature phase (LTP, 303 K), R3PBKC crystallizes in the polar space group *P*1, and the crystal parameter a = 8.8250(3) Å, b = 9.6134(4) Å, c = 13.8807(6) Å, α = 87.117(4)°, β = 87.490(3)°, γ = 67.156(4)°, and V = 1083.50(8) $Å^3$ (Table S2†). The minimum asymmetric unit contains four *R*-3P organic cations and two $[KBiCl_6]^{2-}$ ions (Fig. 1a). Notably, the O atom of the *R*-3P is connected to K forming a coordinated bond that leads the $[KCl_6O_2]^{5-}$ dodecahedron to twist (Fig. S4a†). Interestingly, in the intermediate temperature phase ITP_1 (353 K), R3PBKC remains crystallized in the triclinic system polar space group *P*1. This indicates that LTP to ITP_1 occurs an isomorphic phase transition, with cell parameters a = 8.6922(2) Å, b = 9.3395(3) Å, c = 13.4833(3) Å, α = 86.838(2)°, β = 87.464(2)°, γ = 65.957(3)°, and V = 997.81(5) $Å^3$ (Table S2†). The minimum asymmetric unit of the components in ITP_1 is the same as that in the LTP (Fig. 1a). Although the stacking model remains the same between LTP and ITP_1, slight changes occur in the asymmetric unit, which is reflected in the O–K–O and K–O–C angle changes from 94.38–96.77° and 149.71–154.12° to 60.34–95.47° and 153.52–159.56°, respectively (Fig. 1b, c, and S4b†). To be convenient for the analysis of the ferroelectric origin of R3PBKC, the cations of the four different orientation states were signed A1, A2, A3, and A4. As shown in Fig. S5,† A1, and A4 are polarity aligned along the *b* and *c* axis, respectively. Meanwhile, the polarization components of A2 and A3 cancel each other in the *b*-axis direction, and the residual polarization is superimposed on the *c*-axis. Similarly, there is polarization at the *a*-axis. Therefore, R3PBKC has spontaneous polarization on three axes.

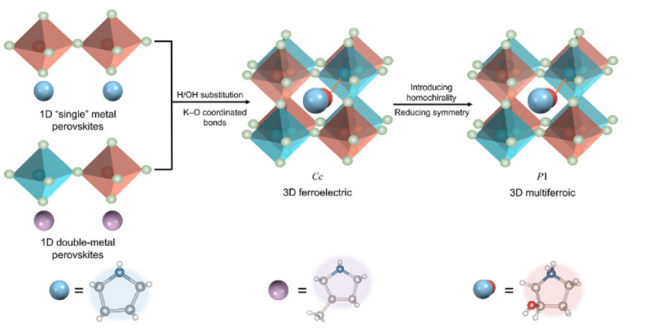

Scheme 1 3D ferroelectrics are designed based on H/OH substitution and K–O coordination bonds, followed by introduction of homochirality to reduce symmetry, yielding 3D multiferroics.

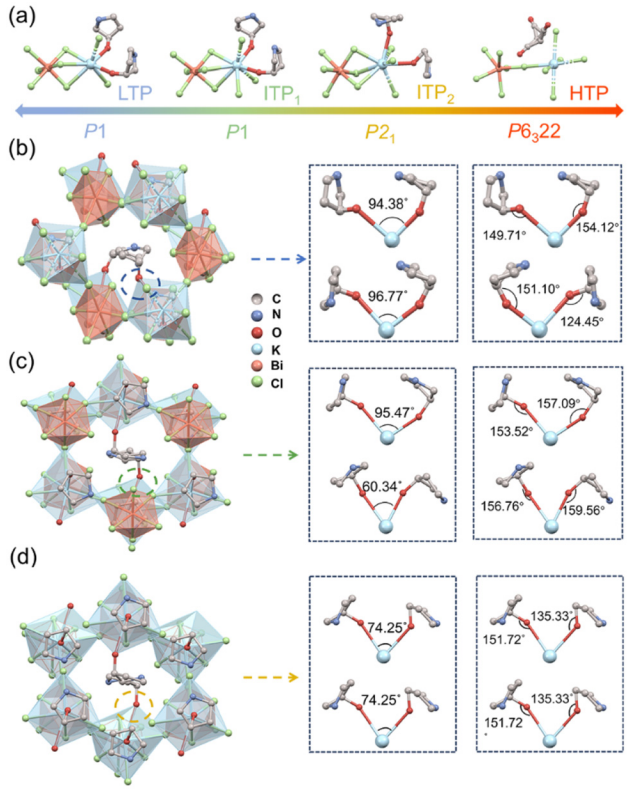

Fig. 1 Minimum asymmetric unit of R3PBKC shown at different temperatures at LTP, ITP_1, ITP_2, and HTP (a). Packing views of R3PBKC at LTP (b), ITP_1 (c), and ITP_2 (d).

In ITP_2 (386 K), R3PBKC crystallized in the monoclinic chiral-polar space group $P2_1$ with point group 2, and the crystal parameters are a = 8.8088(9) Å, b = 13.5482(9) Å, c = 9.3421(12) Å, $\alpha = \gamma = 90°$, β = 115.166(14)°, and V = 1009.1(2) Å^3 (Table S3†). The minimum asymmetric unit consists of two *R*-3P cations and one dodecahedron $[KCl_6O_2]^{5-}$ and one octahedron $[BiCl_6]^{3-}$ (Fig. 1a). At ITP_1, the Cl–Bi–Cl and Cl–K–Cl bond angles are 86.30–178.38° and 66.15–151.75°, respectively. In ITP_2, the Cl–Bi–Cl bond angles change to 86.13–176.61°, and Cl–K–Cl bond angles vary from 63.62 to 146.7° (Fig. S6a and S6b†), which shows slight deformation of the inorganic framework. Furthermore, the O–K–O and K–O–C angle changes from 60.34–95.47° and 153.52–159.56° to 74.25° and 135.33–151.72°, respectively, due to the *R*-3P cation changes significantly from four orientations to two (Fig. 1c and d). Therefore, from ITP_1 to ITP_2, the reorientation of the chiral cations and slight distortion of the double-metal framework induce the SPT.

In the high-temperature phase (HTP, 413 K), R3PBKC crystallized in a higher symmetry hexagonal crystal system ($P6_322$), with unit cell parameters a = 9.3090(15) Å, b = 9.3090(15) Å, c = 13.5171(12) Å, $\alpha = \beta = 90°$, $\gamma = 120°$, and V = 1014.4(3) Å^3 (Table S3†). The minimum asymmetric unit has a highly disordered *R*-3P cation and a $[KBiCl_5]^-$ ion. It is worth noting that the special interaction force of K–O is weakened due to the high disorder of organic cations. The bond length and bond angles show significant changes, which are reflected in the changes in Cl–Bi–Cl and Cl–K–Cl bond angles to 73.51–139.12°, 85.25–174.59°, respectively (Fig. S6c†). Compared with the previous three phases, HTP exhibits much higher symmetry, and organic cations gradually change from an ordered state to a highly disordered state. In addition, the inorganic skeleton gradually changes from a twisted to a highly regular state. Therefore, SPT results from the reorientation changes and order–disorder of the organic cations and the gradual distortion of the inorganic framework.

2.2. Proof of ferroelectricity

To verify the SPT, R3PBKC was investigated using differential scanning calorimetry (DSC). R3PBKC has three pairs of absorption/exothermic peaks around 347 K/317 K (T_{c1}), 376 K/369 K (T_{c2}), and 392 K/386 K (T_{c3}) revealing three SPT in R3PBKC (Fig. 2a). The behavior of reversible SPT can also be verified by temperature-dependent of the dielectric constant. As shown in Fig. 2b, the dielectric anomaly of R3PBKC was measured for the powder samples at different frequencies with temperatures ranging from 300–400 K. The value of the dielectric constant increases with the decrease of frequency at the same temperature, indicating a frequency dependence. During the cooling process, when the frequency is 1 MHz, the real part of the dielectric constant (ε') shows inflection points at T_{c1}, T_{c2}, and T_{c3} temperature points, forming four different plateaus. The illustration in Fig. 2b clearly shows the apparent step-like variation in the dielectric anomaly. The dielectric constants of single-crystal R3PBKC were measured along different axes, and the dielectric anomalies similar to those of the powder sample were observed (Fig. S7†). In addition, the imaginary part of the dielectric constant (ε'') of the powder sample shows a distinct

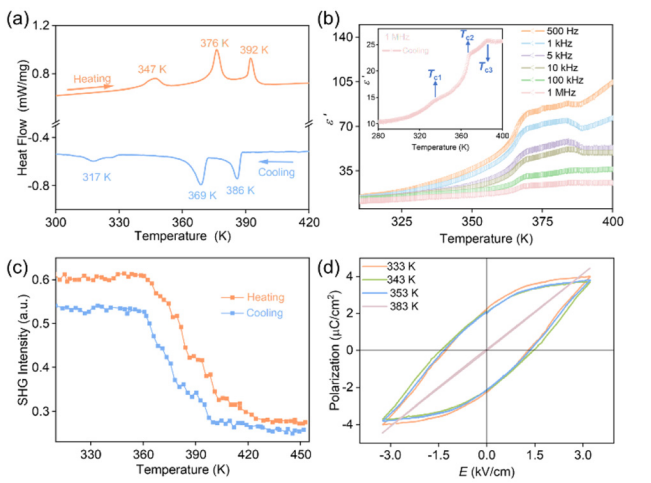

Fig. 2 (a) DSC curves of R3PBKC at 300–420 K. (b) Temperature-dependence of the dielectric constant real part of the powder R3PBKC measured during cooling; inset shows the cooling process at 1 MHz. (c) Temperature-dependence of the SHG intensity for R3PBKC in a heating–cooling cycle. (d) *P*–*E* hysteresis loops of R3PBKC along the *c*-axis measured at 333, 343, 353 K and 383 K.

step-change over the range at 280–400 K, similar to that of the real part (Fig. S8†). It is consistent with the DSC results. Similarly, the reversible phase transitions of PBC, 3MPBKC and 3PBKC were confirmed by DSC measurements and dielectric responses. The DSC measurement results of crystal 3MPBKC showed no reversible SPT behavior (Fig. S9†). However, the DSC curves of PBC and 3PBKC have a pair of absorption/exothermic peaks during heating and cooling, indicating that PBC, 3PBKC undergo reversible SPT. In addition, the dielectric results of PBC and 3PBKC were consistent with the DSC results (Fig. S10†).

The Aizu symbol for R3PBKC can be marked as 2*F*1, and the corresponding symmetry element is reduced from 2 (*E*, C_2) to 1 (*E*). Symmetry breaking was confirmed by second harmonic generation (SHG). A variable-temperature SHG experiment was conducted over the range 310–455 K (Fig. 2c). Specifically, after T_{c2}, the SHG signal decreases from 0.6 to 0.42, which corresponds to the first SPT of R3PBKC, indicating that the space group changes from *P*1 to $P2_1$. In addition, after T_{c3}, SHG exhibits a step-like change, and the relative intensity dropped from 0.32 to 0.23, showing a significant increase in symmetry elements, which is consistent with the result that the space group changed from $P2_1$ to $P6_322$. Overall, the SHG results indicate that symmetry breaking is consistent with space group variation. Notably, the dielectric response and the variable-temperature switching of SHG signals indicate the potential ferroelectricity of R3PBKC.

To verify the ferroelectricity of R3PBKC, its *P*–*E* hysteresis loops were measured using a classical Sawyer-Tower circuit method. As shown in Fig. 2d and S11,† a series of typical *P*–*E* hysteresis loops were recorded at 333, 343, 353 K and 383 K along the *c*-axis. The P_s values of R3PBKC at 333 K along the *a*-, *b*-, and *c*-axis are 3.25, 3.30, and 3.45 μC cm^{-2}, respectively. At 333 K, for a single crystal with a thickness of 2.02 mm, we obtained the coercive field (the intercept of the loop with the field axis) E_c = 1.29 kV cm^{-1}. In addition, when the temperature rises to 383 K, the *P*–*E* hysteresis loop becomes straight. This clearly confirms the existence of a paraelectric phase in R3PBKC. Similarly, we also carried out variable-temperature SHG measurements and *P*–*E* hysteresis loop experiments for 3PBKC, and confirmed the potential ferroelectricity of 3PBKC (Fig. S12†). These results reveal the ferroelectricity of R3PBKC and 3PBKC.

2.3. Proof of ferroelasticity and semiconductor properties

The SPT of R3PBKC can be labeled as 2*F*1 and 622*F*2(s) by the Aizu symbol, which belongs to the 94 known ferroelastic transitions, implying potential ferroelasticity. Under orthogonal polarized light microscopy, ferroelastic materials have different birefringence characteristics, presenting alternating areas of light and dark. To demonstrate the ferroelasticity of R3PBKC, the ferroelastic domain evolution was observed by polarized light microscopy (Movie S1†). First, the morphology of R3PBKC was observed under natural light at 353 K (Fig. 3a). Interestingly, under polarized light, clear ferroelastic domains

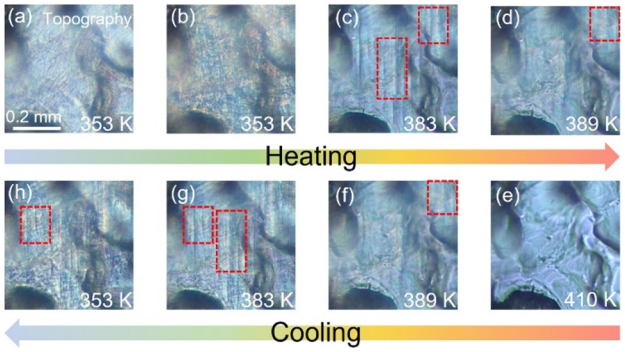

Fig. 3 Temperature-dependent evolution of the ferroelastic domain of R3PBKC. Crystal topography of R3PBKC under natural light. (a) Evolution of the ferroelastic domain under orthogonally polarized light during heating/cooling (b–h).

were observed. As the temperature increases to 383 K (Fig. 3b), the ferroelastic domain-walls decrease significantly, which means that R3PBKC enters the ITP. When the temperature further increases to 410 K, the ferroelastic domain shrinks and disappears, indicating the transition from the ferroelastic phase to the paraelastic phase (Fig. 3c and d). Subsequently, in the process of cooling from 410 K to 353 K (Fig. 3e–h), the ferroelastic domain-walls reappear and expand to the initial state, changing along the order HTP → ITP_2 → ITP_1. The phenomenon of reversible ferroelastic domain wall disappearance and reappearance driven by temperature strongly proves the ferroelasticity of R3PBKC. In addition, Bi-based hybrid double perovskites have potential semiconductor properties,[47] and R3PBKC also exhibits semiconductor behavior. The optical band gap of R3PBKC was determined by solid-state ultraviolet-visible (UV-vis) absorption spectroscopy at room temperature. As shown in Fig. S13,† the absorption edge of R3PBKC appears at 358 nm, and the absorption curve has a clear edge cutoff. According to reports of similar structures, R3PBKC is an indirect band gap semiconductor material. The optical band gap value was determined as 3.18 eV based on the Tauc equation. These results indicate that R3PBKC has semiconductor properties, which shows its potential as a photoelectric semiconductor material.

3. Conclusion

In summary, we successfully obtained a 3D hybrid bimetallic perovskite semiconductor R3PBKC with the lowest symmetry (*P*1) by using H/OH substitution to introduce homochirality and form K–O coordinated bonds. In addition, R3PBKC exhibits ferroelectric and ferroelastic multiferroicity, confirmed by typical *P*–*E* hysteresis loops and reversible ferroelastic domain evolution. Our study provides a new perspective to realize 3D hybrid perovskite multiferroics and gives a deep insight into exploring 3D hybrid multifunctional materials.

Author contributions

L. P. M. conceived the project. Z. J. X. prepared the samples. L. H. S. and H. K. L. performed the PXRD and TG measurements. M. L. R. and Z. A. Q. performed the dielectric measurements. H. Y. Y. and C.S. contributed to single crystal measurement and analysis. N. W. and X. Z. performed the ferroelectric and ferroelastic characterization. Z. J. X. wrote the manuscript, with inputs from all other authors.

Data availability

The datasets supporting this article have been provided as part of the ESI.†

Conflicts of interest

There are no conflicts to declare.

Acknowledgements

L.-P. M. acknowledges the support from National Natural Science Foundation of China (grant no. 22205087 and 22371095) and Natural Science Foundation of Jiangxi Province (no. 20232BAB213003 and 20242BAB23015). N. W. acknowledges the support from the Science and Technology Project of Jiangxi Provincial Department of Education (grant no. GJJ2400711). H.-Y. Y. acknowledges the support from National Natural Science Foundation of China (grant no. 22275075) and Natural Science Foundation of Jiangxi Province (grant no. 20204BCJ22015).

References

1 T.-Y. Ju, C.-C. Fan, B.-D. Liang, C.-D. Liu, M.-L. Jin, C.-Y. Chai and W. Zhang, Chirality Triggered Biferroicity in a 3D Rubidium Based Perovskite, *Adv. Funct. Mater.*, 2024, **34**, 2316747.
2 L.-P. Miao, N. Ding, N. Wang, C. Shi, H.-Y. Ye, L. Li, Y.-F. Yao, S. Dong and Y. Zhang, Direct observation of geometric and sliding ferroelectricity in an amphidynamic crystal, *Nat. Mater.*, 2022, **21**, 1158–1164.
3 C.-W. Nan, M. Bichurin, S. Dong, D. Viehland and G. Srinivasan, Multiferroic magnetoelectric composites: Historical perspective, status, and future directions, *J. Appl. Phys.*, 2008, **103**, 031101.
4 R. Ramesh and N. A. Spaldin, Multiferroics: progress and prospects in thin films, *Nat. Mater.*, 2007, **6**, 21–29.
5 H. Schmid, Multi-ferroic magnetoelectrics, *Ferroelectrics*, 1994, **162**, 317–338.
6 J. Scott, Applications of modern ferroelectrics, *Science*, 2007, **315**, 954–959.
7 H.-K. Li, W. Luo, L. Ye, Z.-J. Xu, M.-L. Ren, C. Shi, H.-Y. Ye, L.-P. Miao and N. Wang, Hybrid Perovskite Molecular Rotor Ferroelastic Semiconductor Constructed by Supramolecular Assembly, *Cryst. Growth Des.*, 2024, **24**, 5411–5416.
8 M. Bichurin, R. Petrov, V. Leontiev, G. Semenov and O. Sokolov, Magnetoelectric current sensors, *Sensors*, 2017, **17**, 1271.
9 H. Chen, D. Hu, Q. Yang, J. Gao, J. Fu, K. Yang, H. He, S. Chen, Z. Kan and T. Duan, All-small-molecule organic solar cells with an ordered liquid crystalline donor, *Joule*, 2019, **3**, 3034–3047.
10 Y. Lee, J. Park, S. Cho, Y.-E. Shin, H. Lee, J. Kim, J. Myoung, S. Cho, S. Kang and C. Baig, Flexible ferroelectric sensors with ultrahigh pressure sensitivity and linear response over exceptionally broad pressure range, *ACS Nano*, 2018, **12**, 4045–4054.
11 K. Zhai, D.-S. Shang, Y.-S. Chai, G. Li, J.-W. Cai, B.-G. Shen and Y. Sun, Room-temperature nonvolatile memory based on a single-phase multiferroic hexaferrite, *Adv. Funct. Mater.*, 2018, **28**, 1705771.
12 C.-C. Fan, X.-B. Han, B.-D. Liang, C. Shi, L.-P. Miao, C.-Y. Chai, C.-D. Liu, Q. Ye and W. Zhang, Chiral Rashba ferroelectrics for circularly polarized light detection, *Adv. Mater.*, 2022, **34**, 2204119.
13 P. Gao, J. Britson, J. R. Jokisaari, C.-T. Nelson, S.-H. Baek, Y. Wang, C.-B. Eom, L.-Q. Chen and X. Pan, Atomic-scale mechanisms of ferroelastic domain-wall-mediated ferroelectric switching, *Nat. Commun.*, 2013, **4**, 2791.
14 E. Sawaguchi, Y. Akishige, T. Yamamoto and J. Nakahara, Phase transition in hexagonal type BaTiO3, *Ferroelectrics*, 1989, **95**, 29–36.
15 J.-F. Scott and C. A. Paz de Araujo, Ferroelectric memories, *Science*, 1989, **246**, 1400–1405.
16 P. Siwach, P. Sikarwar, J.-S. Halpati and A.-K. Chandiran, Design of above-room-temperature ferroelectric two-dimensional layered halide perovskites, *J. Mater. Chem. A*, 2022, **10**, 8719–8738.
17 A. Wang, C. Zhang, Q. Guan, H. Ye, R. Li, H. Li, Y. Geng, C. Qu, Z. Wang and C. Ji, Polar 3D Perovskitiod Constructed by Asymmetric Diamine for Stable Self-Driven X-Ray Detection, *Small*, 2024, 2407843.
18 H.-Y. Zhang, X.-G. Chen, Z.-X. Zhang, X.-J. Song, T. Zhang, Q. Pan, Y. Zhang and R.-G. Xiong, Methylphosphonium tin bromide: a 3D perovskite molecular ferroelectric semiconductor, *Adv. Mater.*, 2020, **32**, 2005213.
19 W. Zhang and R.-G. Xiong, Ferroelectric metal-organic frameworks, *Chem. Rev.*, 2012, **112**, 1163–1195.
20 P.-P. Shi, S.-Q. Lu, X.-J. Song, X.-G. Chen, W.-Q. Liao, P.-F. Li, Y.-Y. Tang and R.-G. Xiong, Two-dimensional organic-inorganic perovskite ferroelectric semiconductors with fluorinated aromatic spacers, *J. Am. Chem. Soc.*, 2019, **141**, 18334–18340.
21 A.-S. Tayi, A. Kaeser, M. Matsumoto, T. Aida and S.-I. Stupp, Supramolecular ferroelectrics, *Nat. Chem.*, 2015, **7**, 281–294.
22 T. Zhang, K. Xu, J. Li, L. He, D.-W. Fu, Q. Ye and R.-G. Xiong, Ferroelectric hybrid organic-inorganic perovs-

kites and their structural and functional diversity, *Natl. Sci. Rev.*, 2023, **10**, nwac240.
23 H.-K. Li, L.-P. Wang, Z.-Z. Cui, Q. Xu, L.-L. Zou, N. Wang, L.-P. Miao, H.-Y. Ye and C. Shi, A series of bimetallic ammonium RbEu nitrates exhibiting switchable dielectric constant and photoluminescence properties, *J. Mater. Chem. C*, 2024, **12**, 14122–14128.
24 A.-K. Jena, A. Kulkarni and T. Miyasaka, Halide perovskite photovoltaics: background, status, and future prospects, *Chem. Rev.*, 2019, **119**, 3036–3103.
25 M.-M. Lee, J. Teuscher, T. Miyasaka, T.-N. Murakami and H.-J. Snaith, Efficient hybrid solar cells based on meso-superstructured organometal halide perovskites, *Science*, 2012, **338**, 643–647.
26 J. Lin, M. Lai, L. Dou, C.-S. Kley, H. Chen, F. Peng, J. Sun, D. Lu, S.-A. Hawks and C. Xie, Thermochromic halide perovskite solar cells, *Nat. Mater.*, 2018, **17**, 261–267.
27 J.-S. Manser, J.-A. Christians and P.-V. Kamat, Intriguing optoelectronic properties of metal halide perovskites, *Chem. Rev.*, 2016, **116**, 12956–13008.
28 C.-C. Stoumpos and M.-G. Kanatzidis, Halide Perovskites: poor Man's high-performance semiconductors, *Adv. Mater.*, 2016, **28**, 5778–5793.
29 N. Wang, H.-K. Li, H.-Y. Shen, L. Ye, Z.-J. Xu, M.-L. Ren, N.-T. Yao, C. Shi, H.-Y. Ye and L.-P. Miao, Supramolecular Rotor Assembly for the Design of a Hybrid Ferroelectric-Antiferromagnetic Multiferroic Semiconductor, *Angew. Chem., Int. Ed.*, 2024, e202421298.
30 H.-Y. Zhang, X.-J. Song, H. Cheng, Y.-L. Zeng, Y. Zhang, P.-F. Li, W.-Q. Liao and R.-G. Xiong, A three-dimensional lead halide perovskite-related ferroelectric, *J. Am. Chem. Soc.*, 2020, **142**, 4604–4608.
31 M.-E. Kamminga, G.-A. de Wijs, R.-W. Havenith, G.-R. Blake and T.-T. Palstra, The role of connectivity on electronic properties of lead iodide perovskite-derived compounds, *Inorg. Chem.*, 2017, **56**, 8408–8414.
32 X. Li, Y. He, M. Kepenekian, P. Guo, W. Ke, J. Even, C. Katan, C.-C. Stoumpos, R. D. Schaller and M. G. Kanatzidis, Three-dimensional lead iodide perovskitoid hybrids with high X-ray photoresponse, *J. Am. Chem. Soc.*, 2020, **142**, 6625–6637.
33 X. Li, M. Kepenekian, L. Li, H. Dong, C.-C. Stoumpos, R. Seshadri, C. Katan, P. Guo, J. Even and M.-G. Kanatzidis, Tolerance factor for stabilizing 3D hybrid halide perovskitoids using linear diammonium cations, *J. Am. Chem. Soc.*, 2022, **144**, 3902–3912.
34 R. Liu, Y. Yu, C. Liu, H. Yang, X.-L. Shi, H. Yu and Z.-G. Chen, A-site cation engineering enables oriented Ruddlesden-Popper perovskites towards efficient solar cells, *Sci. China: Chem.*, 2022, **65**, 2468–2475.
35 S. Cao, K. Kuang, B. He, J. Tang, Z. Yu, M. Li, Y. He and J. Chen, Methylated diammonium spacer modulated three-dimensional lead bromide perovskitoid hybrids with distinct photoconductivity anisotropy, *Inorg. Chem. Front.*, 2024, **11**, 4270–4276.
36 H.-Y. Liu, H.-Y. Zhang, X.-G. Chen and R.-G. Xiong, Molecular design principles for ferroelectrics: ferroelectrochemistry, *J. Am. Chem. Soc.*, 2020, **142**, 15205–15218.
37 X. Mu, H.-Y. Zhang, L. Xu, Y.-Y. Xu, H. Peng, Y.-Y. Tang and R.-G. Xiong, Ferroelectrochemistry, *APL Mater.*, 2021, **9**, 051112.
38 Y. Ai, X.-G. Chen, P.-P. Shi, Y.-Y. Tang, P.-F. Li, W.-Q. Liao and R.-G. Xiong, Fluorine substitution induced high T_c of enantiomeric perovskite ferroelectrics:(R)-and (S)-3-(fluoropyrrolidinium) $MnCl_3$, *J. Am. Chem. Soc.*, 2019, **141**, 4474–4479.
39 Z.-X. Wang, Y. Zhang, Y.-Y. Tang, P.-F. Li and R.-G. Xiong, Fluoridation achieved antiperovskite molecular ferroelectric in $[(CH_3)_2(F\text{-}CH_2CH_2)NH]3(CdCl_3)(CdCl_4)$, *J. Am. Chem. Soc.*, 2019, **141**, 4372–4378.
40 K. Aizu, Possible species of "ferroelastic" crystals and of simultaneously ferroelectric and ferroelastic crystals, *J. Phys. Soc. Jpn.*, 1969, **27**, 387–396.
41 P.-P. Shi, S.-Q. Lu, X.-J. Song, X.-G. Chen, W.-Q. Liao, P.-F. Li, Y.-Y. Tang and R.-G. Xiong, Two-dimensional organic-inorganic perovskite ferroelectric semiconductors with fluorinated aromatic spacers, *J. Am. Chem. Soc.*, 2019, **141**, 18334–18340.
42 N. Wang, Z.-J. Xu, H.-F. Ni, W. Luo, H.-K. Li, M.-L. Ren, C. Shi, H.-Y. Ye, X.-B. Fu and Y. Zhang, Molecular Engineering Regulation Achieving Out-of-Plane Polarization in Rare–Earth Hybrid Double Perovskites for Ferroelectrics and Circularly Polarized Luminescence, *Angew. Chem.*, 2024, **136**, e202409796.
43 Y.-L. Zeng, X.-Q. Huang, C.-R. Huang, H. Zhang, F. Wang and Z.-X. Wang, Unprecedented 2D Homochiral Hybrid Lead-Iodide Perovskite Thermochromic Ferroelectrics with Ferroelastic Switching, *Angew. Chem., Int. Ed.*, 2021, **60**, 10730–10735.
44 Y.-A. Xiong, T.-T. Sha, Q. Pan, X.-J. Song, S.-R. Miao, Z.-Y. Jing, Z.-J. Feng, Y.-M. You and R.-G. Xiong, A nickel(II) nitrite based molecular perovskite ferroelectric, *Angew. Chem.*, 2019, **131**, 8949–8953.
45 Z.-J. Xu, W. Luo, H.-K. Li, M.-L. Ren, C. Shi, N. Wang, H.-Y. Ye and L.-P. Miao, Multiaxial Multiferroicity with Large Spontaneous Polarization in a Hydroxyl-Modified Quinuclidinium Gallium(III) Chloride, *Chem. Mater.*, 2024, **36**, 7595–7603.
46 J. Zhou, P. Xie, C. Wang, T. Bian, J. Chen, Y. Liu, Z. Guo, C. Chen, X. Pan and M. Luo, Hybrid Double Perovskite Derived Halides Based on Bi and Alkali Metals (K, Rb): Diverse Structures, Tunable Optical Properties and Second Harmonic Generation Responses, *Angew. Chem., Int. Ed.*, 2023, **62**, e202307646.
47 C.-F. Wang, H. Li, M.-G. Li, Y. Cui, X. Son, Q.-W. Wang, J.-Y. Jiang, M.-M. Hua, Q. Xu, K. Zhao, H.-Y. Ye and Y. Zhang, Centimeter-Sized Single Crystals of Two-Dimensional Hybrid Iodide Double Perovskite $(4,4\text{-Difluoropiperidinium})_4AgBiI_8$ for High-Temperature Ferroelectricity and Efficient X-Ray Detection, *Adv. Funct. Mater.*, 2021, **31**, 2009457.

